Peer-reviewed version available at *Sensors* **2018**, *18*, 2152; doi:10.3390/s18072152

Article

InSAR Baseline Estimation for Gaofen-3 Real-Time DEM Generation

Huan Lu [1], Zhiyong Suo[1,*], Zhenfang Li [1], Jinwei Xie [1], and Qingjun Zhang [2]

[1] National Laboratory of Radar Signal Processing, Xidian University, Xi'an, 710071, China; luhuanohyeah@126.com (H.L.); lzf@xidian.edu.cn; jerryxie9@gmail.com (J.X.);
[2] Beijing Institute of Spacecraft System Engineering, China Academy of Space Technology, Beijing 100094, China; zhangqj@cast.cn
* Correspondence: zysuo@xidian.edu.cn; Tel.: +86-29-88202248

Abstract: For Interferometry Synthetic Aperture Radar (InSAR), the normal baseline is one of the main factors that affect the accuracy of the ground elevation. For Gaofen-3 (GF-3) InSAR processing, the poor accuracy of the real-time orbit determination resulting in a large baseline error, leads to the modulation error in azimuth and the slope error in range for timely Digital Elevation Model (DEM) generation. In order to address this problem, a novel baseline estimation approach based on Shuttle Radar Topography Mission (SRTM) DEM is proposed in this paper. Firstly, the orbit fitting is executed to remove the non-linear error factor, which is different from traditional methods. Secondly, the height errors are obtained in slant-range plane between SRTM DEM and the GF-3 generated DEM which can be used to estimate the baseline error with a linear variation. Then, the real-time orbit can be calibrated by the baseline error. Finally, the DEM generation is performed by using the modified baseline and orbit. This approach has the merit of spatial and precise orbital free ability. Based on the results of GF-3 interferometric SAR data for Hebei, the effectiveness of the proposed algorithm is verified and the accuracy of GF-3 real-time DEM products can be improved extensively.

Keywords: GF-3; InSAR; DEM; baseline estimation; real-time orbit

---

1. Introduction

The baseline is an important parameter in InSAR that affects the accuracy of the surface elevation, which is defined as the distance between the two antenna phase centers that illuminate the same area [1]. The accuracy of calibration parameters plays an important role for real-time DEM generation in some special conditions, such as the natural disasters. Hence, it is a great challenge to improve the accuracy of the baseline which is taken as an important parameter in calibration.

A variety of estimation algorithms have been studied to improve the accuracy of the baseline. So far, many satellite-based InSAR baseline estimation methods have been studied. The basic and typical algorithms [2] of baseline estimation are the satellite orbit state vector method, the external control points method, and the Fast Fourier Transformation (FFT) method.

The satellite orbit state vector method uses the satellite ephemeris parameters to obtain baseline parameters through the vector difference between the two satellite positions. However, the precision of baseline cannot be guaranteed because it is affected greatly by the satellite positioning. Zheng et al. [3] proposed a method of orbital linear fitting to satisfy the precision of spaceborne InSAR interference measurement, which has higher accuracy than the general method by original orbit. Nevertheless, the accuracy of it cannot be promised under the real-time orbit.

The external control points method uses the ground control points (GCPs) with known elevation information and interferometric phase, and combines the equations of the interferometric system to obtain the baseline parameters with high accuracy [4]. Du et al. [5] studied the estimation of baseline parameters of space-borne InSAR based on GCPs, and the method was tested with ENVISAT ASAR data for Dujiangyan region of Sichuan Province of China. A new estimation algorithm with block

Peer-reviewed version available at *Sensors* **2018**, *18*, 2152; doi:10.3390/s18072152

adjustment considering the phase offset for multiple InSAR data that covers large areas was proposed to reduce the number of ground control points and the difference between heights derived from different data [6]. The experiments of baseline estimation with block adjustment are explored with multiple pairs of InSAR data obtained by airborne InSAR system were experimentally verified by Institute of Electronics, Chinese Academy of Sciences with less ground control points. In [7], an accurate method for determining the precise interferometric baseline was provided with the aid of the least squares estimation by using ground control points. However, the number of GCPs must be enough and the computation is extensive. The method is only applicable to data with GCPs and the scope of application is limited.

The FFT initial estimation method is based on the frequency information of flat interference fringes to determine calibration parameters. Singh et al. [8] proposed a method that the baseline parameters can be retrieved from a Fourier analysis of the interferometric fringes. Xu et al. [9] proposed a novel high precision spaceborne InSAR baseline estimation approach based on interferometric fringe frequency which makes improvements from two aspects: the baseline calculation formula and the fringe frequency estimation precision. However, the selected data area should be flat in this method. Therefore, a large measurement error will exist for some uneven areas or special circumstances such as earthquakes.

In addition, a lot of works about baseline estimation have been studied except traditional methods. Jin et al. [11] proposed an initial baseline estimation of InSAR based on the phases of flat earth. A calibration estimation method [12] which uses co-registration offsets and non-linear least square algorithm was proposed, but the vertical baseline is inaccurate. Two ENVISAT SLC (Single Look Complex) images covering Tibet, China were applied to test this method. In terms of the vertical effective baseline, Chen et al. [13] proposed an estimation of InSAR baseline based on the Frequency Shift Theory. In addition, there is an estimation method based on subspace projection [14]. It is highly robust to the unwrapping phase and can restrain the noise well, but the information about some points on the ground was used in this method. A new approach for interferometric calibration was proposed [15,16], based on the idea of maximizing the correlation between the original complex interferogram and reference values of it obtained from ground control points. The main advantage with respect to traditional techniques is that the method does not require the phase to be unwrapped in advance, and the method is computationally more demanding than traditional techniques.

However, the research angle of these approaches is the physical baseline or vertical effective baseline. Different from them, our method makes use of SRTM DEM to estimate the parallel baseline instead of the physical baseline or vertical baseline. It comes along with the following advantages: the modulation error in azimuth can be demonstrated clearly because its variation tendency is basically in line with the parallel baseline change, and the “slope” error in range can be obtained directly. Besides, our method has no need for corner reflectors and no restriction to flat terrain in the scenes. Therefore, the terrain information can be obtained timely and accurately with our method under earthquake conditions.

In this paper, a novel method of baseline estimation based on SRTM DEM for real-time DEM generation is proposed and the effectiveness of the approach is verified by using GF-3 satellite data for Hebei area, which is the first time to use this method for GF-3 interferometric processing. Firstly, the preprocessing which is called orbit fitting is performed to remove the non-linear error factor according to the characters of GF-3 real-time orbits, and there is no pretreatment before estimating calibration parameters in the conventional methods. Then, considering of the “slope” effect in GF-3 interferometric processing, the physical baseline is decomposed to analyze the main source of the problem, and then the accuracy of the DEM product can be improved by correcting the parallel baseline component instead of the physical baseline. In addition, the error of estimation is linear instead of a constant as opposed to some general methods so that the DEM product is more reliable. Finally, from the scope of application, our method will not be affected by GCPs, topography and orbit accuracy. Therefore, the approach presented herein can obtain terrain information with high accuracy during natural disasters such as earthquakes. And it can provide direct data support to help the post-earthquake emergency commanders and staff understand the landscape of the earthquake area.

Peer-reviewed version available at Sensors 2018, 18, 2152; doi:10.3390/s18072152

The remainder of this paper is organized as follows: Section 2 explains the InSAR processing chain briefly, then the principle and flow of the baseline estimation for real-time DEM generation by SRTM DEM are given after analyzing the baseline errors. In Section 3, the experiments on two GF-3 SAR images are conducted to validate the effectiveness and efficiency of the proposed method. Finally, the conclusions are drawn in Section 4.

2. Principle and Methods

2.1. Principle and InSAR Processing

The basic principle of DEM generation uses two SAR antennas with interferometric imaging capabilities (or repeatable observation of one antenna) to acquire two coherent single-look complex images in the same region with certain different looking angles. We can get the elevation of the surface by the phase information, thereby reconstructing the DEM of the corresponding area [17,18].

It is difficult for a single platform to adjust two antennas at the same time on account of the limitation of spaceborne platform. In general, the repeat-pass single antenna is used to obtain the interference images for spaceborne interferometric radars. It is difficult to ensure proper baseline parameters because the ground conditions and scattering characteristics may have changed due to a time interval between two images. GF-3 satellite is the repeat-pass mode, and the operating mode is shown in Figure 1.

As demonstrated in Figure 1, the elevation of the antenna phase center A_1 is H , and the elevation of the ground point P is h . θ indicates the side looking angle, B denotes the baseline of the distance between the two antennas, α is the angle between B and the horizontal direction, R and $R^{'}$ are the slant-range from the two antenna phase centers to the target point P respectively, and ΔR represents the corresponding slant-range difference.

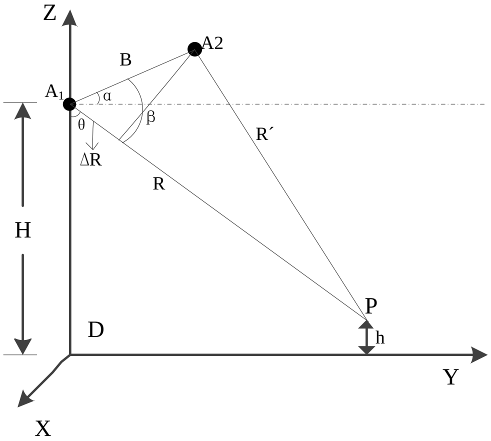

Figure 1. Repeat-pass work mode.

On the basis of the geometry of Figure 1 and the cosine theorem, the elevation h of the ground point P is denoted as:

$$h = H - R\cos\theta = H - R\cos(90^\circ + \alpha - \arccos(-\frac{\Delta R}{B} + \frac{B}{2R} - \frac{\Delta R^2}{2RB})) \qquad (1)$$

From the foregoing description, it can be seen that the geometrical principle of InSAR for measuring terrain height is not complicate and it has some problems with the implementation. On the one hand, it is hard to obtain two highly coherent SAR images for the same scene. On the other hand, the true value of the interferometric phase cannot be obtained directly from the complex image, which makes the InSAR process chain become complex. The basic flow for establishing the ground height model by using the interferometric method for elevation measurement is demonstrated in Figure 2.

Peer-reviewed version available at Sensors 2018, 18, 2152; doi:10.3390/s18072152

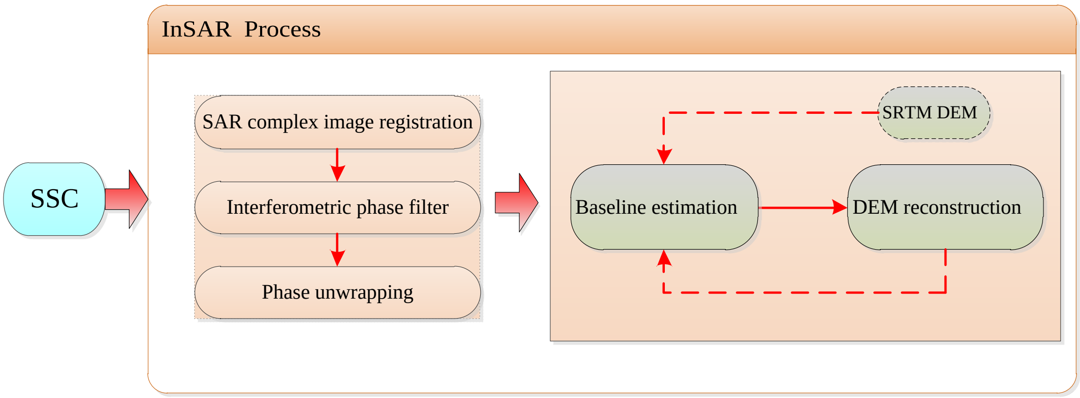

Figure 2. InSAR technical flow chart.

In Figure 2, SSC represents the Slant-range Single-look Complex SAR image. SAR complex image registration [19,20] is a critical step in InSAR processing, and the geometric registration [21] is used to obtain the phase of interference. Virtually, many noises will lead to phase discontinuities. Therefore, filtering must be performed to remove noises in order to improve the signal-to-noise ratio (SNR). MUSIC mode [22] can be used to remove noise. Throughout the technical process, phase unwrapping is an important technology, and there are many efficient methods to unwrap phase [23,24,25]. It is worth mentioning that the interference phase and the absolute interference phase generated after unwrapping still differ from the absolute phase by a number of entire cycles. The relationship is expressed as follows:

$$\phi_{abs} = \phi_{unw} + 2k\pi \tag{2}$$

where ϕ_{abs} means absolute phase, ϕ_{unw} is the unwrapping phase, and k presents the absolute fuzzy number which can be obtained by the external DEM. Therefore, the absolute phase must be obtained to complete the final phase-altitude conversion.

After the process above, the topographic information will be obtained which can be used in some special conditions such as earthquake and other natural calamities. At the same time, the scientific orbital data acquired after tens of days cannot guarantee the timeliness of obtaining the geomorphic information for rescuers. Therefore, the real-time orbit must be corrected in some methods to obtain higher-precision DEM products.

SAR complex image registration, interferometric phase filter, and phase unwrapping are important aspects of interferometric processing. They're just briefly introduced since they're not the focus of the study. The following focuses on baseline estimation and DEM generation. It is the key of generating DEM to build a proper model and exactly eliminate the influence of baseline error.

2.2. Baseline Error Analysis

Baseline is a three-dimensional vector with multiple decomposition methods, and the two most common decomposition manners are shown in Figure 3. The first pattern is that the three coordinate directions are along the heading B_a, the cutting heading B_c and the radial direction B_r respectively. The second decomposition is that the three coordinates are along the heading B_a, along the line of sight direction B_p and the vertical line of sight $B_\perp$ respectively.

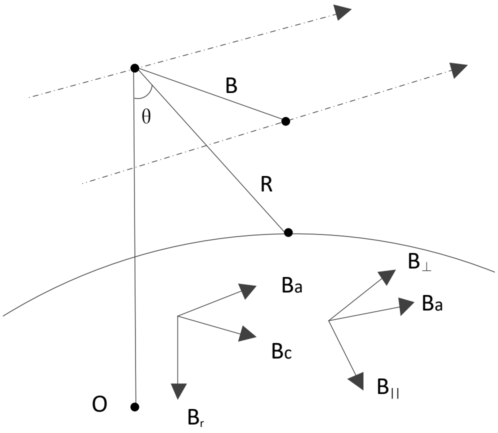

Figure 3. Baseline and the different forms.

In general, the first decomposition method is used to describe the accuracy of ephemeris parameters, while the second decomposition is often used for InSAR system performance analysis and it will be employed in this paper. The image coherence, height sensitivity and the measurement accuracy are affected by baseline error directly. Therefore, the influence of $\Delta B_\perp$, ΔB_a and ΔB_p on DEM accuracy[26] will be analyzed separately before coming up the method of baseline estimation in this paper.

1) Baseline error of $\Delta B_\perp$

The relationship between the elevation of the target point and the phase after removing the flattening effect in the self-transmit and self-received mode is defined as follows:

$$h = h_{amb}\frac{\phi}{2\pi} = \frac{\lambda R\sin\theta}{2B_\perp}\frac{\phi}{2\pi} \tag{3}$$

where h_{amb} means the height of ambiguity which represents the parameter that causes elevation changes by phase changes, λ denotes the wavelength, θ is the look angle, R indicates the slant range, and ϕ represents the unwrapping phase after removing the flattening effect. The elevation can be formulated under a baseline measurement error in $\Delta B_\perp$ as follows:

$$\hat{h} = \hat{h}_{amb}\frac{\phi}{2\pi} = \frac{\lambda R\sin\theta}{2(B_\perp+\Delta B_\perp)}\frac{\phi}{2\pi} \tag{4}$$

Therefore, the height error introduced by $\Delta B_\perp$ can be expressed as follows [28,29]:

$$\begin{aligned}\Delta h = \hat{h} - h &= \frac{\lambda R\sin\theta}{2(B_\perp+\Delta B_\perp)}\frac{\phi}{2\pi} - \frac{\lambda R\sin\theta}{2B_\perp}\frac{\phi}{2\pi}\\ &= \frac{\lambda R\sin\theta(B_\perp - B_\perp - \Delta B_\perp)}{2(B_\perp+\Delta B_\perp)B_\perp}\frac{\phi}{2\pi}\\ &= -\frac{\lambda R\sin\theta\Delta B_\perp}{2(B_\perp+\Delta B_\perp)B_\perp}\frac{\phi}{2\pi}\\ &= -h\frac{\Delta B_\perp}{B_\perp+\Delta B_\perp} \approx -h\frac{\Delta B_\perp}{B_\perp}\end{aligned} \tag{5}$$

Generally, $\Delta B_\perp$ is about several millimeters, while $B_\perp$ is around several hundred meters. Hence, we can get $\frac{\Delta B_\perp}{B_\perp} \approx 10^{-5}$. At the same time, the maximum height h of the earth is less than 9000m. Therefore, the height error introduced by $B_\perp$ is in the level of centimeter and can be ignored.

2) Baseline error of ΔB_a

As shown in the Figure 4, MS and MS' represent the true and measured values of the baseline, respectively, SV is the vertical baseline component, and SS' represents the baseline error along the heading. Assuming that the InSAR system uses zero Doppler imaging in the processing, it has the following form:

$$\left.\begin{array}{l} MV \perp SS' \\ MV \perp SV \end{array}\right\} \Rightarrow MV \perp SVS' \Rightarrow S'V \perp MV \tag{6}$$

where MV is the parallel baseline (which determines the interference phase) of MS and MS'. As a result, even though there is a measurement error along the heading baseline, the interferometric phase equation, the slant range equation, and the Doppler equation [27] which affect the DEM generation are not changed. Therefore, the error of ΔB_a can be negligible on height accuracy [28,29].

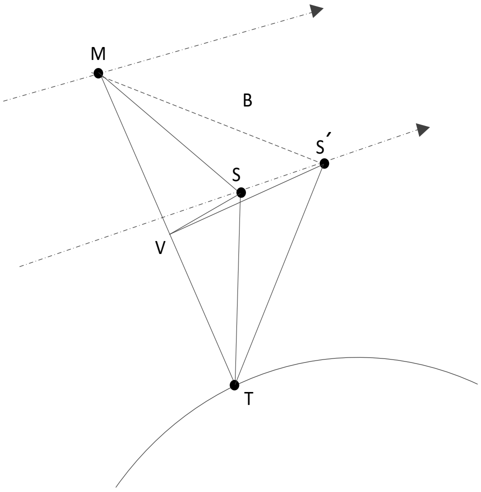

Figure 4. Baseline measurement error geometrical diagram.

3) Baseline error of ΔB_{P}

In spaceborne interferometric geometry, the baseline length is much smaller than the slant range, and B_{P} equals the one-way wave path-difference of the electromagnetic wave. Therefore, the height error caused by the baseline measurement error of B_{P} can be denoted as [30]:

$$\Delta h = h_{amb}\frac{2\Delta B_{\mathrm{P}}}{\lambda} \tag{7}$$

From Equation (7), the accuracy of the elevation will be affected by ΔB_{P}. In addition, the ΔB_{P} will bring about a slope error in range because the height of ambiguity h_{amb} varies along the distance. The corresponding slope is defined as:

$$\begin{aligned} k_{tilt} &= \frac{\Delta h_{far} - \Delta h_{near}}{R_{far}\sin\theta_{far} - R_{near}\sin\theta_{near}} \\ &= \frac{\frac{\lambda R_{far}\sin\theta_{far}}{2B_{\perp}}\frac{2\Delta B_{\mathrm{P}}}{\lambda} - \frac{\lambda R_{near}\sin\theta_{near}}{2B_{\perp}}\frac{2\Delta B_{\mathrm{P}}}{\lambda}}{R_{far}\sin\theta_{far} - R_{near}\sin\theta_{near}} \\ &= \frac{\Delta B_{\mathrm{P}}}{B_{\perp}} \end{aligned} \tag{8}$$

where R_{near} and R_{far} denote the proximal and distal distance respectively, θ_{near} and θ_{far} indicate the proximal and distal angles of view, $\Delta h_{far} - \Delta h_{near}$ is the difference between the proximal and distal

Peer-reviewed version available at Sensors 2018, 18, 2152; doi:10.3390/s18072152

elevation, and $R_{far}\sin\theta_{far} - R_{near}\sin\theta_{near}$ represents the distance between the proximal and distal distance. The elevation error varies in meters and a relative elevation error is generated in a $1°\times1°$ range of DEM (approximate $10^5 m$ in ground-range) because of $\frac{\Delta B_p}{B_p} \approx 10^{-5}$.

According to the analysis above and the equations, the main factor which causes DEM precision loss is ΔB_p. Therefore, an appropriate model should be built to correct the ΔB_p so as to generate a higher precision DEM.

2.3. The Proposed Method

The error of B_p will result in the modulation error in azimuth and the slope error [31] in range for DEM generation. Figure 5 displays the process chain of baseline estimation by SRTM DEM. On account of a poor accuracy of the real-time orbit in GF-3 data, orbit fitting is the preprocessing before baseline estimation. In this way, the non-linear error factor will be removed and some rules of the baseline change can be observed clearly. It is critical for obtaining baseline error to acquire the elevation error between SRTM DEM and GF-3 generated DEM in slant-range plane. In addition, in order to acquire a higher precision DEM product, the baseline error correction is critical. After correcting the linear variation error, a more precise orbits and DEM product can be obtained. Finally, the DEM generation is performed which can verify the result of our baseline estimation. The procedure of the proposed approach is given in details.

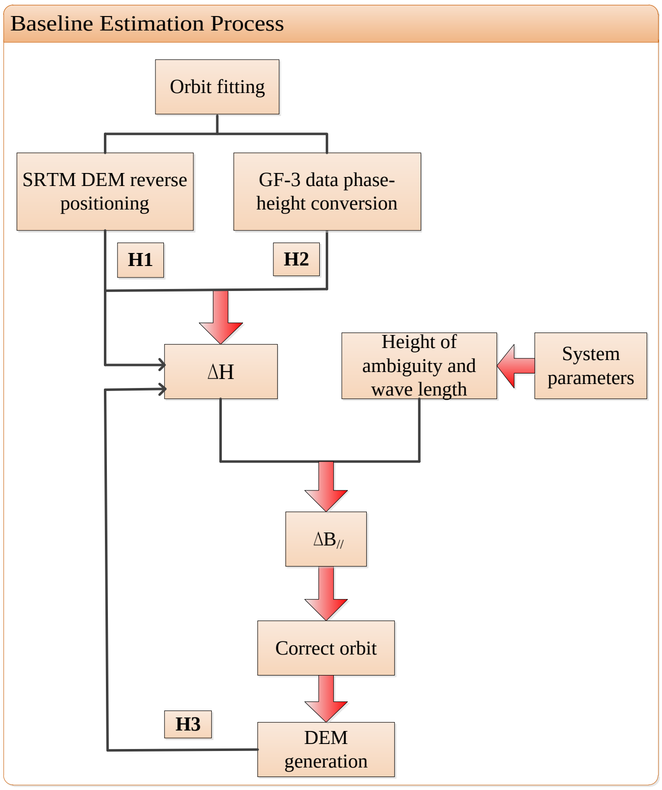

Figure 5. Baseline estimation with SRTM DEM.

2.3.1. Orbit fitting

It is hard to obtain the baseline error accurately due to the low accuracy of the real-time orbit determination of GF-3 data. Therefore, orbit fitting must be performed in order to wipe out the non-linear error factor. The Lagrange polynomial curve fit method [32] with acceptable feasibility and accuracy will be used to perform it. The Lagrange interpolation polynomial can be expressed as follows:

$$
\begin{aligned}
&L(x)=\sum_{j=0}^{k} y_j l_j(x) \\
&l_j(x)=\prod_{i=0,i\neq j}^{k}\frac{x-x_i}{x_j-x_i}=\frac{x-x_0}{x_j-x_0}\cdots\frac{x-x_{j-1}}{x_j-x_{j-1}}\frac{x-x_{j+1}}{x_j-x_{j+1}}\cdots
\end{aligned}
\tag{9}
$$

where x_j represents the independent variable, y_j corresponds to the value of the function at x_j, and $l_j(x)$ is the interpolation cardinal function. After orbit fitting, some inaccurate orbit positions will be calibrated.

2.3.2. Elevation error in slant-range plane

It shows that the baseline error is closely related to the elevation error from Equation (7). Thus the elevation error between SRTM DEM and the GF-3 generated DEM in slant-range plane must be obtained. The inverse positioning is proposed which includes three steps to obtain the height of SRTM DEM in slant-range plane.

1) Coordinate conversion

SRTM DEM provides three-dimensional coordinates of the latitude, longitude and elevation in ground-plane, whereas the information for each point in slant-range plane is usually implemented in the WGS84 (World Geodetic System−1984 Coordinate System) coordinate system. Specially, coordinate must be transformed for the sake of finding corresponding positions of SRTM DEM in slant-range plane. The conversion relationship can be displayed as follows:

$$
\begin{cases}
X=(N+H)\cos B\cos L \\
Y=(N+H)\cos B\sin L \\
Z=(N(1-e^2)+H)\sin B \\
N=a(1-e^2\sin^2 B)^{-1/2}
\end{cases}
\tag{10}
$$

where X, Y and Z represent the coordinates in WGS84 coordinate system, B means north latitude, L indicates longitude, H is the height, N demotes the radius of curvature in prime vertical of the point, a illustrates the Semi-major Axis, and e^2 represents the first eccentricity. After the conversion of Formula [10], the matching WGS84 coordinate of each position can be acquired.

2) SRTM DEM interpolation

Generally speaking, the height matrix size obtained by SRTM DEM is much smaller than the size of GF-3 image. In order to get a more accurate elevation value after the reverse positioning, the elevation matrix generated by the SRTM DEM should be interpolated. In the experiment, the original elevation matrix is interpolated into an elevation matrix of $2\times Na\times 2\times Nr$ (Na and Nr are the number of azimuth and range pixels respectively).

3) Obtain the elevation of SRTM DEM in slant-range plane

The position in azimuth of each point in slant-range plane will be obtained through the focused Doppler center, and the location in range will be acquired by combining the sampling interval and slant range from the parameter file. Then the elevation of SRTM DEM in slant-range plane will be received by reverse positioning. Finally, the height matrix should be interpolated based on the azimuth and distance pixels for several inaccurate elevation.

However, the elevation of GF-3 data in slant-range plane is achieved by means of target location with Newton iterative method [33,34] which is different from the reverse positioning method. The three-dimensional position information of any point in the scene will be obtained by solving the slant range equation, interferometric phase equation, and Doppler equation [27,35]. According to InSAR geometric model in Section 2.1, positioning equation can be expressed as follows:

Peer-reviewed version available at *Sensors* **2018**, *18*, 2152; doi:10.3390/s18072152

$$\begin{cases} \left|\vec{S_1}-\vec{P}\right| = R_1 \\ \left|\vec{S_2}-\vec{P}\right| = R_2 \\ f_{dc1} = -2(\vec{S_1}-\vec{P})\cdot(\vec{V_{S1}}-\vec{V_P})/(\lambda R_1) \end{cases} \tag{11}$$

where S_1 is the phase center of the transmitting antenna (namely master antenna), S_2 is the phase center of the receiving antenna (namely slave antenna), P represents the ground target, λ represents the wavelength, $\vec{V_{S1}}$ indicates the master antenna's velocity vector, $\vec{V_P}$ is the velocity vector of the ground target point, and f_{dc1} illustrates the imaging Doppler center frequency of the master antenna. The above equations can be defined as follows:

$$\begin{aligned} &(x_1-x)^2+(y_1-y)^2+(z_1-z)^2 = R_1{}^2 \\ &(x_2-x)^2+(y_2-y)^2+(z_2-z)^2 = R_2{}^2 \\ &f_{dc} = -\frac{2\left[(x_1-x)\mathrm{V}_x+(y_1-y)V_y+(z_1-z)V_z\right]}{\lambda R_1} \end{aligned} \tag{12}$$

where (x_1,y_1,z_1) and (x_2,y_2,z_2) are the coordinates of S_1 and S_2 respectively, (x,y,z) represents the coordinates of P , and (V_x,V_y,V_z) is the speed of the master antenna. The system of equations is a ternary quadratic system of equations that can be solved using the Newton iteration method.

Non-linear equations can be defined as:

$$f = \begin{pmatrix} f_1(x_1,x_2,\ldots,x_n) \\ f_2(x_1,x_2,\ldots,x_n) \\ \vdots \\ f_n(x_1,x_2,\ldots,x_n) \end{pmatrix} \tag{13}$$

The linear phase can be developed and obtained by the Taylor formula of the multivariate function and it has the following forms:

$$\begin{pmatrix} f_1^{(k)}\left(x_1^{(k)},x_2^{(k)},\ldots,x_n^{(k)}\right) \\ f_2^{(k)}\left(x_1^{(k)},x_2^{(k)},\ldots,x_n^{(k)}\right) \\ \vdots \\ f_3^{(k)}\left(x_1^{(k)},x_2^{(k)},\ldots,x_n^{(k)}\right) \end{pmatrix} + f'(\mathrm{x}^{(k)}) \begin{pmatrix} x_1^{(k+1)}-x_1^{(k)} \\ x_2^{(k+1)}-x_2^{(k)} \\ \vdots \\ x_n^{(k+1)}-x_n^{(k)} \end{pmatrix} = 0 \tag{14}$$

$$f'(\mathrm{x}) = \begin{pmatrix} \frac{\partial f_1}{\partial x_1} & \frac{\partial f_1}{\partial x_n} \\ & \\ \frac{\partial f_n}{\partial x_1} & \frac{\partial f_n}{\partial x_n} \end{pmatrix} \tag{15}$$

Equation (13)~ Equation (15) can be written as:

$$\begin{pmatrix} x_1^{(k+1)} \\ x_2^{(k+1)} \\ \vdots \\ x_n^{(k+1)} \end{pmatrix} = \begin{pmatrix} x_1^{(k)} \\ x_2^{(k)} \\ \vdots \\ x_n^{(k)} \end{pmatrix} - \left[f'(\mathrm{x}^{(k)})\right]^{-1} \begin{pmatrix} f_1^{(k)}\left(x_1^{(k)},x_2^{(k)},\ldots,x_n^{(k)}\right) \\ f_2^{(k)}\left(x_1^{(k)},x_2^{(k)},\ldots,x_n^{(k)}\right) \\ \vdots \\ f_3^{(k)}\left(x_1^{(k)},x_2^{(k)},\ldots,x_n^{(k)}\right) \end{pmatrix} \tag{16}$$

Peer-reviewed version available at Sensors 2018, 18, 2152; doi:10.3390/s18072152

The above formulas can be used to iterate the true ground coordinates and elevation of the target point, and then recover the real terrain through grid interpolation. The implementation flow chart is exhibited in Figure 6.

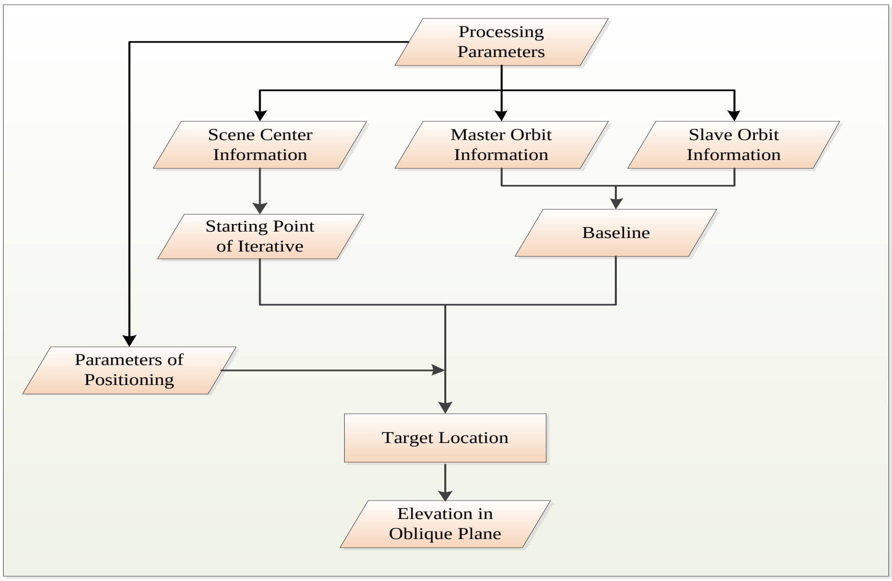

Figure 6. Target location by iterative method.

2.3.3. Baseline error estimation

As can be seen in Formula (7), the height of ambiguity is written as:

$$h_{amb} = \frac{\lambda R \sin\theta}{2B_{\perp}} \tag{17}$$

From Formula (7), the ΔB_p will be acquired by the elevation error, the height of ambiguity and the wave length. In this paper, ΔB_p shows a linear variation instead of a constant estimated in other methods. It is worth noting that the error is not under ECR (Earth-Fixed Coordinate System) coordinate system, while the orbit position is obtained under the ECR coordinate system. Therefore, it is necessary to implement coordinate conversion when correcting the orbit by baseline error.

2.3.4. Orbit correction

The coordinate system of orbits is showed in Figure 7. $O-XYZ$ denotes the ECR coordinate system, N represents the North Pole, Z axis coincides with the earth's rotation axis, and S represents the radar antenna whose position vector and radar velocity vector are $\mathbf{p}_S = (x_1, y_1, z_1)$ and $\mathbf{v}_s = (v_x, v_y, v_z)$ respectively. The position of the sub-satellite point is S', and P represents the ground target whose position vector is $\mathbf{p}_p = (x, y, z)$.

On the basis of the baseline vector coordinate system is demonstrated in Figure 3, we convert ΔB_p to the ECR coordinate system and obtain the triaxial component. And the orbit will be calibrated based on this component.

Peer-reviewed version available at Sensors 2018, 18, 2152; doi:10.3390/s18072152

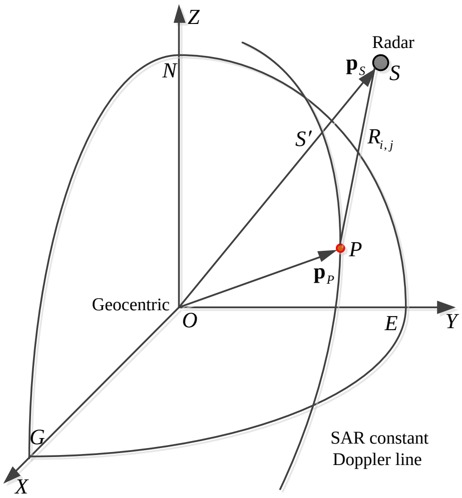

Figure 7. ECR coordinate system.

In this paper, the accuracy of the DEM product is used as an indicator to verify the baseline correction. Therefore, DEM generation should be performed after baseline and orbit correction.

2.3.5. DEM generation

DEM is the main product of InSAR processing [36]. DEM generation consists of two parts: target location and geocoding [37]. Target location has already been introduced as mentioned earlier. The geocoding process projects the elevation on the slant-range plane into the ground-range plane to provide the final DEM product.

Geocoding is similar to the method for obtaining the elevation of the SRTM DEM in slant-plane, and it includes coordinate transformation and data resampling as well. However, the geocoding completes the conversion from the slant-plane to ground-plane which is opposed from the approach proposed to obtain the external DEM in slant-plane.

Figure 8 presents the geocoding model [37].

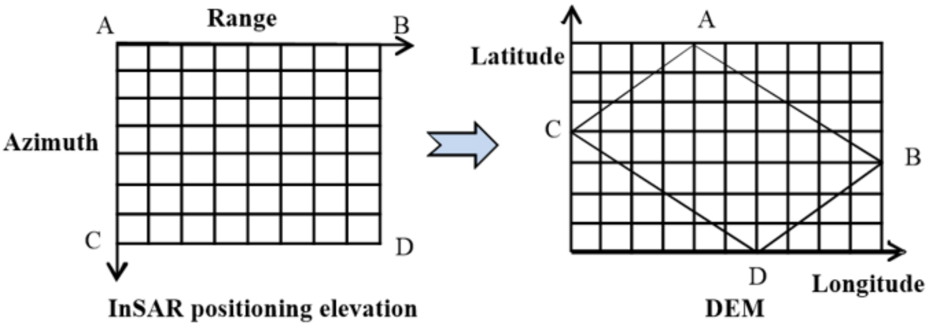

Figure 8. Geocoding model.

In order to represent the difference between our method and the traditional methods more directly, we show four different aspects of processing of the baseline estimation, i.e., the baseline form, preprocessing, the baseline error and limiting conditions, to carry out a system and comparative study. In terms of the research of baseline form, in general, the traditional baseline estimation calculates the physical baseline B and the horizontal angle α .The parallel baseline will be estimated in our method because it is the key source of "slope" effect in GF-3 interference processing. The second difference is that there is no preprocessing in other approaches. Then, what is noteworthy is that the error is a constant in other methods, while it is linear in our approach. In addition, our approach has no limits of orbits, GCPs and terrain. Table 1 shows the details of comparison between the proposed approach and three conventional methods.

Peer-reviewed version available at *Sensors* **2018**, *18*, 2152; doi:10.3390/s18072152

Table 1. Methods comparison.

Methods	Processing			
	Baseline Form	Preprocessing	Baseline Error	Limiting Conditions
Orbit State Vector	Physical baseline and α	No	Constant	Accurate orbits
External Control Points	Physical baseline and α	No	Constant	GCPs
FFT	Physical baseline and α	No	Constant	Flat terrain
Our Method	Parallel baseline	Yes	Linear	No above limits

3. Experimental Results

3.1. Experimental Data

In order to achieve InSAR process effectively, image pair in the same area must have good coherence. After extensive selection and testing of GF-3 SAR images, a pair of images are selected after interception of the public area which are shown in Figure 9.

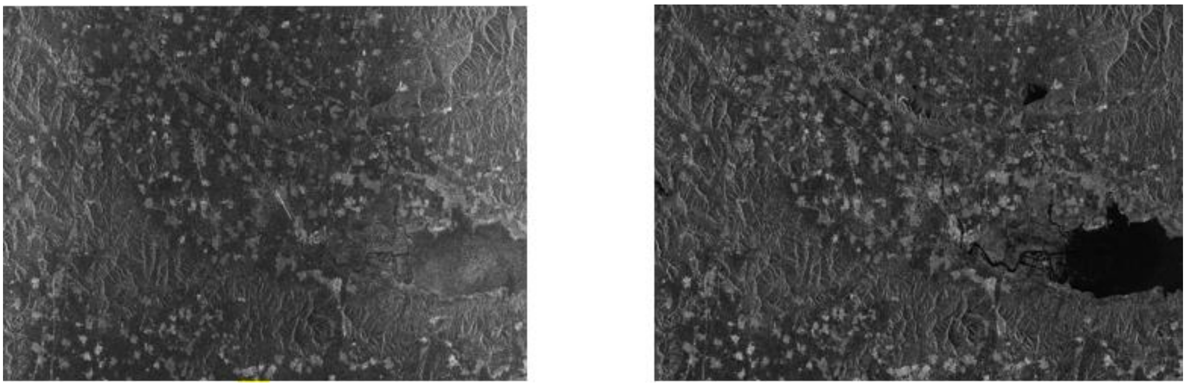
(**a**) (**b**)

Figure 9. Experimental data: (a) the master image of the experiment; (b) the slave image of the experiment.

The main parameters of the data used in the experiment are shown in Table 2.

Table 2. The basic Information about the two GF-3 SAR images employed in the experiment.

Parameter	**Image #1**	**Image #2**
Region	**Hebei**	**Hebei**
Wave length(m)	0.055517	0.055517
Satellite direction	Descending	Desceding
Center frequency(GHz)	5.400012	5.400012
PRF(Pulse Recurrence Frequency)(Hz)	2158.034424	2158.17407
Average altitude(m)	83.756627	25.202458
Look direction	Right	Right
Size(Az × Rng)(pixel)	9311 × 14827	9311 × 14827
Product level	1	1
Product format	TIFF	TIFF

3.2. Results of Baseline Estimation

3.2.1. Results of no correction

Peer-reviewed version available at Sensors 2018, 18, 2152; doi:10.3390/s18072152

Figure 10 shows the result of GF-3 DEM generation without any correction and the topography in Golden Software Surfer.

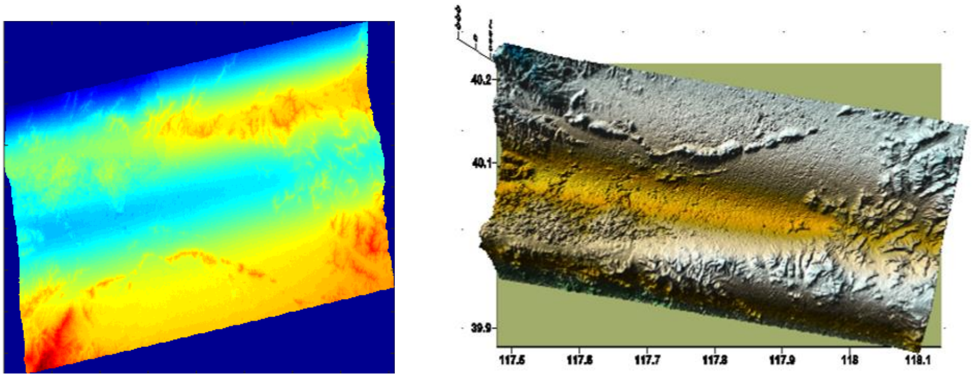

(**a**) (**b**)

Figure 10. DEM product: (**a**) GF-3 generated DEM with no baseline error correction; (**b**) the topography in Surfer of (a).

In Figure 10b, the horizontal direction represents the longitude, the vertical direction indicates the latitude, and the direction which is perpendicular to both the longitude and the latitude illustrates the elevation range. Figure 11 shows the results of Figure 10b after rotating at a certain visual angle so as to observe the elevation changes. At the same time, the SRTM DEM in this area is compared with the GF-3 generated DEM.

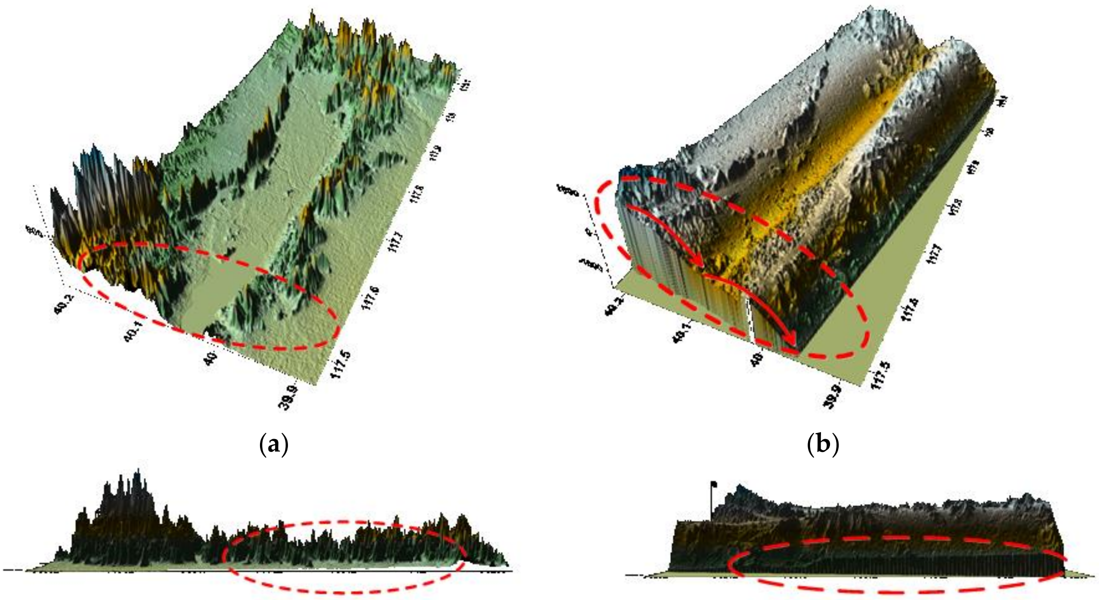

(**a**) (**b**)

(**c**) (**d**)

Figure 11. DEM product after rotating a suitable angle in Surfer: (**a**) SRTM DEM along the latitude; (**b**) GF-3 generated DEM along the latitude; (**c**) SRTM DEM along the longitude; (**d**) GF-3 generated DEM along the longitude.

As can be seen in Figure 11, both latitude and longitude directions have errors if there is no correction, and a large elevation error exists while comparing with SRTM DEM.

3.2.2. Results of baseline error

According to Figure 10a, different error curves which are shown in Figure 12 can be obtained over the entire scene.

Peer-reviewed version available at Sensors 2018, 18, 2152; doi:10.3390/s18072152

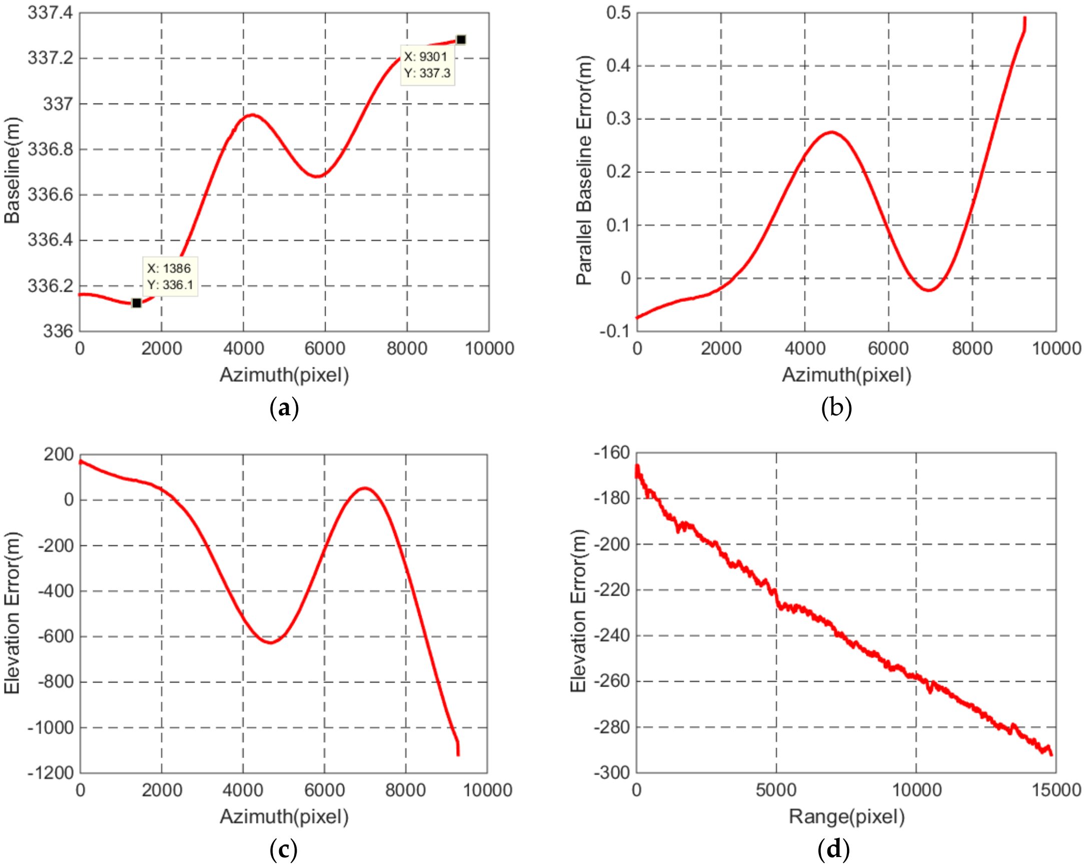

Figure 12. Different error curves: (a) description of the baseline length; (b) description of the parallel baseline error; (c) description of the vertical error in azimuth between SRTM DEM and the GF-3 generated DEM; (d) description of the vertical error in range between SRTM DEM and the GF-3 generated DEM.

As can be seen from the two points marked in Figure 12a, the baseline changes reach to $1.2m$. From Figure 12b, the parallel baseline error is up to $10^{-1}m$, which is too large to generate a high-precision DEM. The elevation error curve in azimuth in Figure 12c shows the same tendency as the elevation changes in azimuth in Figure 11b, while it exhibits and an approximately linear change in range in Figure 12d. All the results in Figure 12 indicate that the baseline error will lead to the slope error in range and the modulation error in azimuth.

3.2.3. Results of orbit fitting

According to Figure 12, the baseline error varies greatly on account of the poor accuracy of the real-time orbit, and Figure 13 shows the DEM generation after orbit fitting by Lagrange polynomial curve fit.

Peer-reviewed version available at *Sensors* **2018**, *18*, 2152; doi:10.3390/s18072152

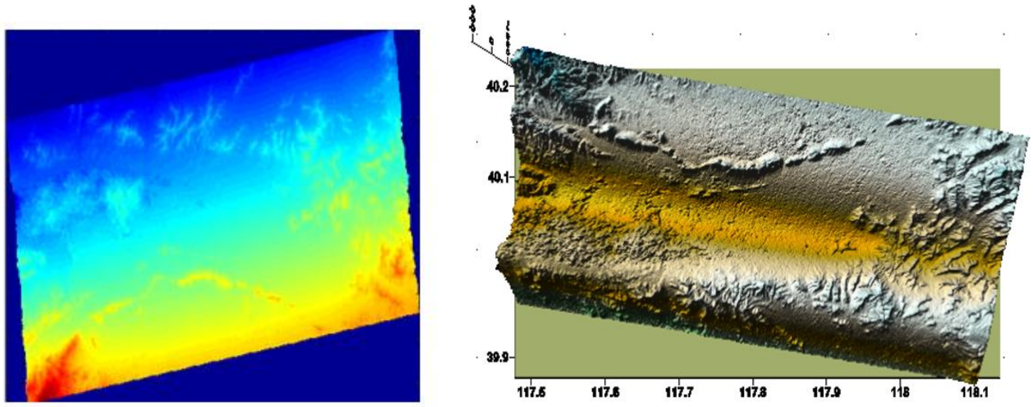

(**a**) (**b**)

Figure 13. DEM generation by fitting orbit: (a) DEM product after geocoding; (**b**) topography in Surfer.

In order to observe the elevation, Figure 13b is rotated in a suitable visual angle and the result is shown in Figure 14.

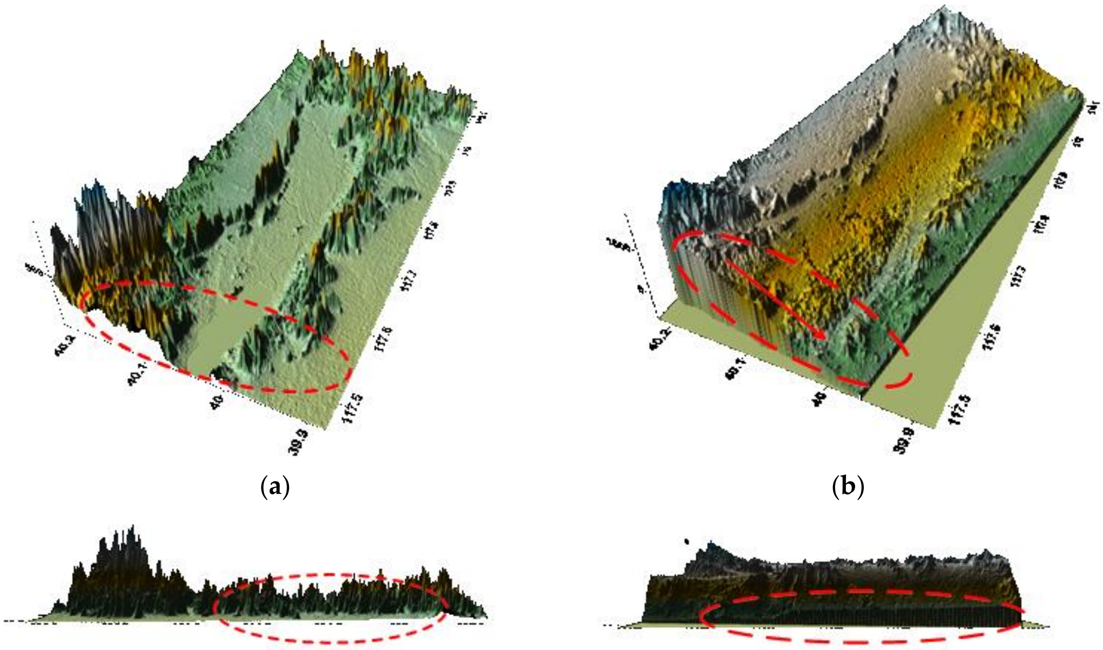

(**a**) (**b**)

(**c**) (**d**)

Figure 14. DEM product after orbit fitting and rotating a suitable angle in Surfer: (**a**) SRTM DEM along the latitude; (**b**) GF-3 generated DEM along the latitude; (**c**) SRTM DEM along the longitude; (**d**) GF-3 generated DEM along the longitude.

After orbit fitting, the error changes in latitude approximately linearly as shown in Figure 14b, which facilitates the subsequent baseline error estimation. And there is a slope error in Figure 14d by comparing Figure 14c. Thus the baseline must be calibrated.

3.2.4. Results of correction

Based on the process flow in Figure 5, we use the fitted orbital information to estimate the elevation error, then the ΔB_p will be estimated and the orbit will be calibrated. In the end, DEM generation will be carried out and the correction results will be verified by observing the height error.

Figure 15 shows the results when the ΔB_p is calibrated for the first time.

Peer-reviewed version available at *Sensors* **2018**, *18*, 2152; doi:10.3390/s18072152

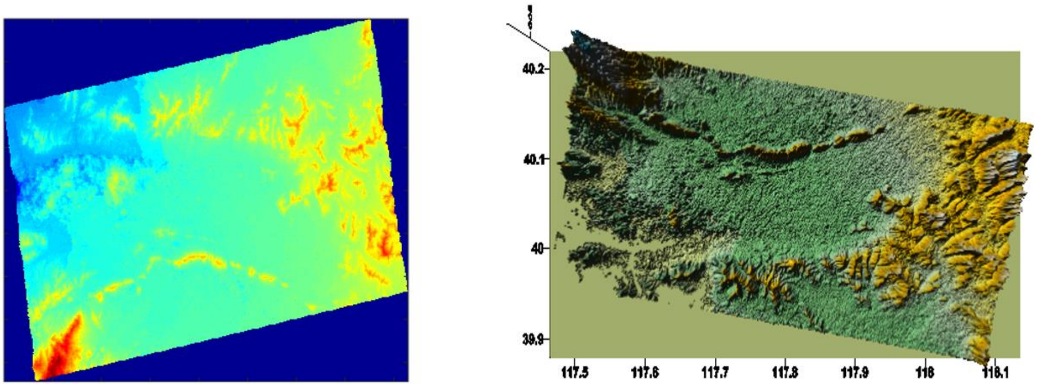

(**a**) (**b**)

Figure 15. DEM generation by correcting baseline error for the first time: (**a**) DEM product after geocoding; (**b**) topography in Surfer.

The DEM product accuracy has an obvious improvement and the terrain information is fully displayed from Figure 15. Similarly, we rotate a certain visual angle so that the error can be showed up.

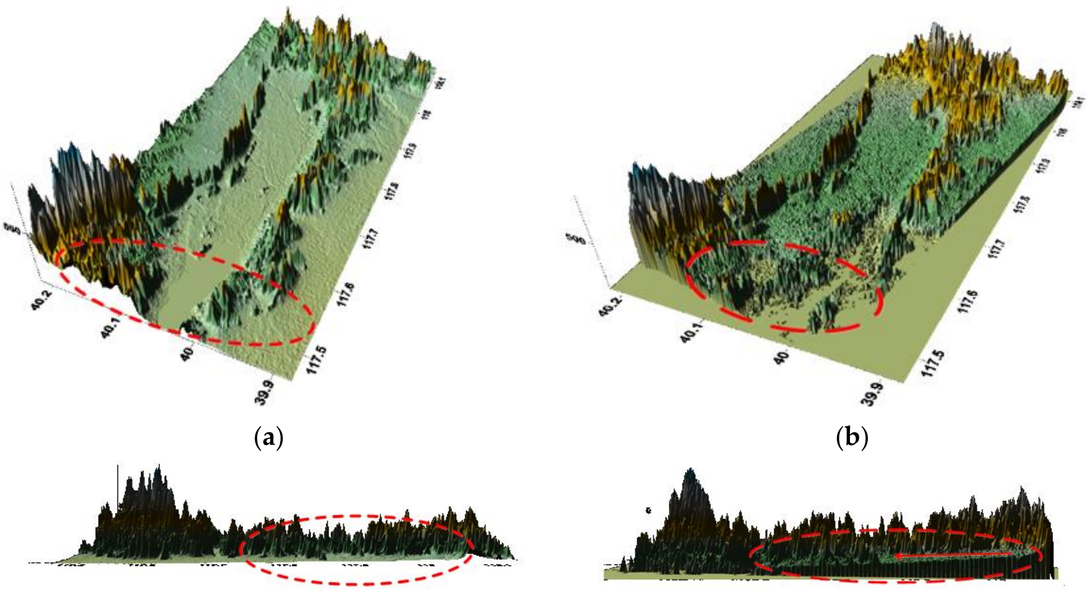

(**a**) (**b**)

(**c**) (**d**)

Figure 16. DEM product after correcting ΔB_p and rotating a suitable angle in Surfer: (**a**) SRTM DEM along the latitude; (**b**) GF-3 generated DEM

The error along the latitudinal direction has been corrected by comparing Figure 16a and Figure 16b with Figure 14b. While there is still a slight slope error and Figure 16d displays the difference. Therefore, the baseline must be estimated for the second time to enhance the DEM's accuracy of convergence. We make use of elevation information which is shown in Figure 15 to re-estimate the ΔB_p and to perform DEM generation. At the same time, the difference of height errors will be observed during the experiment.

Peer-reviewed version available at Sensors 2018, 18, 2152; doi:10.3390/s18072152

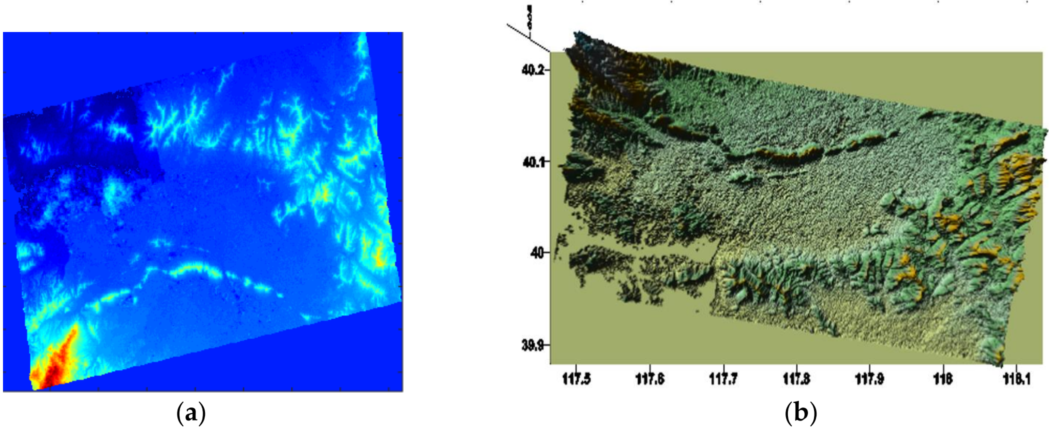

Figure 17. DEM generation by correcting ΔB_p for the second time: (**a**) DEM product after geocoding; (**b**) topography in Surfer.

Figure 17 shows the result when the error is calibrated for the second time. In order to visually observe the slope error, the DEM product has been rotated in a certain visual angle which is displayed in Figure 18.

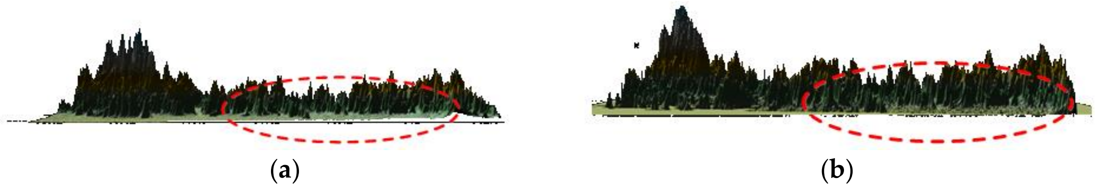

Figure 18. DEM product after correcting baseline error for the second time and rotating a suitable angle in Surfer: (**a**) SRTM DEM; (**b**) GF-3 generated DEM.

As can be seen from Figure 18, there is no slope error. Therefore, the modulation error and the slope error have been calibrated after correction. At the same time, we draw the parallel baseline error during the entire process in Figure 19.

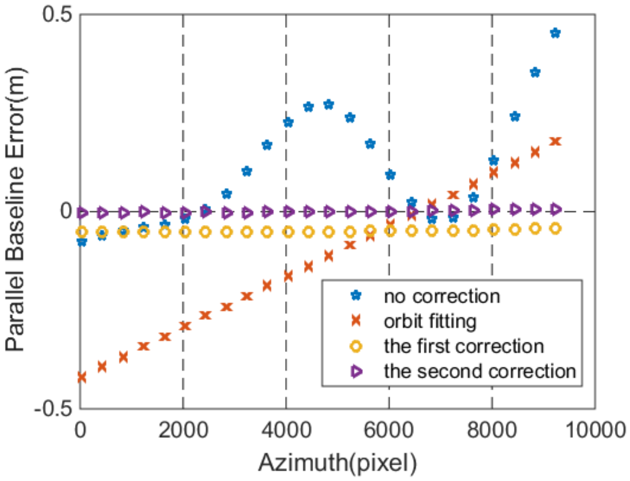

Figure 19. Parallel baseline error comparison.

From Figure 19, it is evident that the ΔB_p is around zero after the second correction. The results indicate that the ΔB_p have been calibrated by SRTM DEM, which benefits the real-time DEM generation.

Peer-reviewed version available at *Sensors* **2018**, *18*, 2152; doi:10.3390/s18072152

Finally, four strong scattering points from the classical landcovers, i.e., the farmland, the village, the urban area, and water body, are selected to demonstrate the high accuracy of DEM generation with the method of baseline estimation. Figure 20 exhibits the positions of the four points in the GF-3 SAR image.

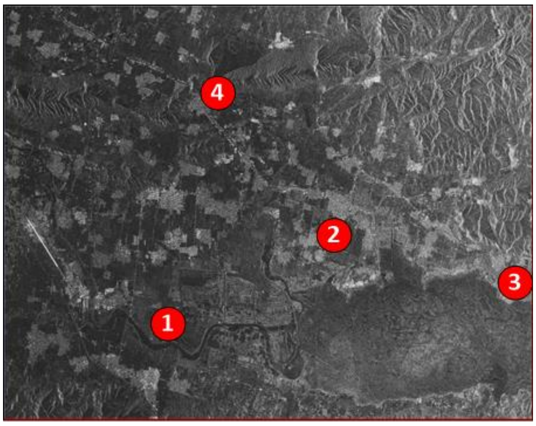

Figure 20. Scattering points in SAR image.

In order to display the details of the scattering points, the four different areas aforementioned are cropped out after geocoding with the SAR image in Figure 20. From Figure 21a to Figure 21d, the points are the junction of the farmland, the crossroad of the village, the crossroad of the city and the strong scattering point around the water body. All the points are marked with red cross. Correspondingly, the optical points are pinned up in Google earth map showing in Figure 21e to Figure 21f. On purpose of presenting the effectiveness of the proposed method, the elevations in Google earth map and the GF-3 generated DEMs of the four points are provided in Table 3.

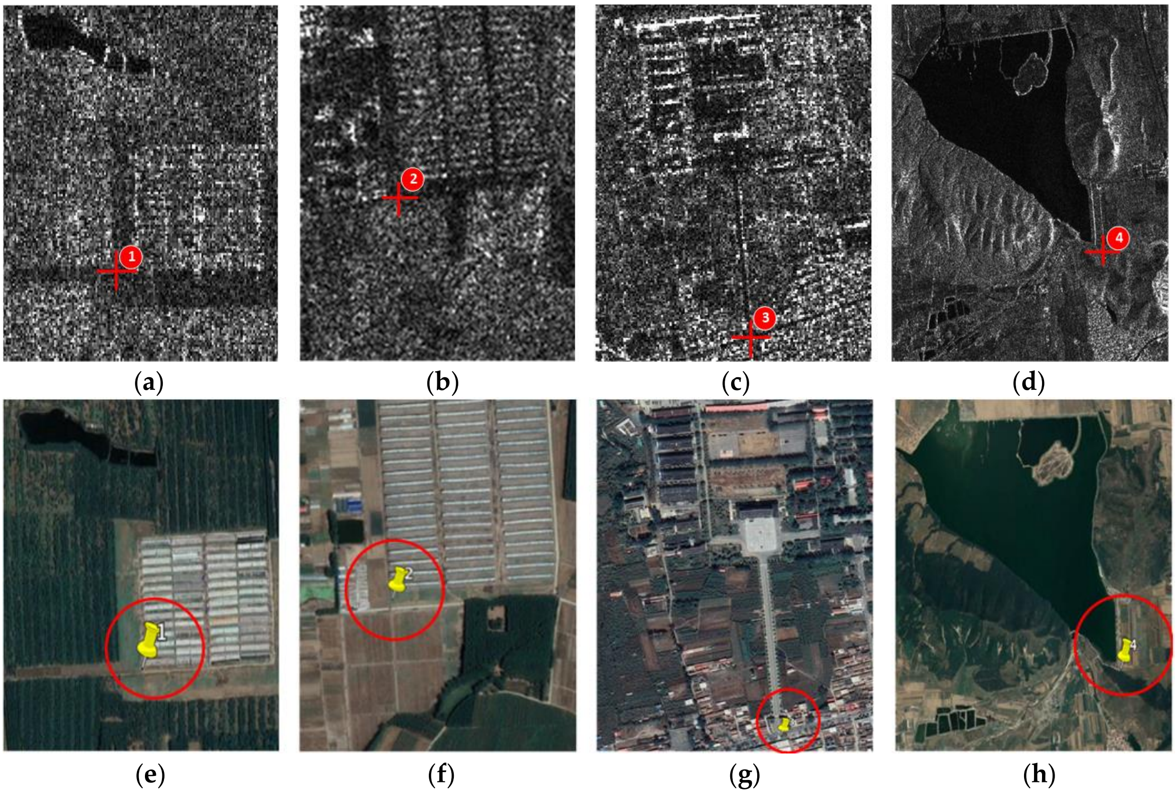

Figure 21. Scattering points: (**a**) the junction of the farmland; (**b**) the crossroad of the village; (**c**) the crossroad of the city; (**d**) the strong scattering point around the water area; (**e**~**h**) four check points on Google Earth.

Peer-reviewed version available at Sensors 2018, 18, 2152; doi:10.3390/s18072152

As shown in Table **3**, the elevation errors of the scattering points are within 3 meters apart from scattering point 1 in our approach. However, the error can cover tens and hundreds of meters with the satellite orbit state vector method due to the poor accuracy of real-time orbit, which indicates that the approach proposed in the paper is executable for obtaining the terrain information with high accuracy for real-time DEM generation.

Table 3. Results of the checking points.

Scattering points	Google Earth(m)	Our method(m)	Satellite Orbit State Vector(m)
1	20	14.1387	74.9312
2	27	25.4709	129.0772
3	81	84.7393	176.2719
4	33	32.6492	144.7998

4. Conclusions

In some special circumstances such as earthquakes, it is necessary to acquire the topographic information quickly. However, the acquisition of scientific orbits requires a certain amount of time and the real-time orbit with poor accuracy will be used for DEM reconstruction, which makes a large baseline error and a low measuring precision. This paper proposes an InSAR baseline estimation method for GF-3 real-time DEM generation based on SRTM DEM. In this experiment, the modulation error has been corrected after the first baseline estimation. However, the slope error still exists so that the error is implemented iteratively to achieve a higher accuracy DEM. After error correction, not only the modulation error and the slope error are calibrated, but also the accuracy of the generated DEM is improved significantly. It's worth noting that the error is a constant in traditional methods which is not enough to generate a high-precision DEM. Therefore, the method proposed in this paper obtains the baseline error with a linear least-squares fit, which is equivalent to estimating a linear variation of the error. In the end, four points in Google Earth are used to verify our results and the error is within a few meters, which makes our method more practical for GF-3 real-time DEM generation, and the terrain can be reproduced and provide direct data support to help the post-earthquake emergency commanders and staff understand the landscape of the earthquake area.

Author Contributions: Huan Lu and Zhiyong Suo conceived the idea. Huan Lu designed the experiment and wrote the manuscript. Zhenfang Li revised the manuscript and gave some suggestions to the analysis. Jinwei Xie provided some practical materials. Zhiyong Suo supervised the experiment. Qingjun Zhang provided great help for the experimental conduction. All approved the final version of the manuscript.

Funding: This work was supported by the National Natural Science Foundation of China (NSFC) under Grant No.61471276, 61671355 and 61601298.

Conflicts of Interest: The authors declare no conflict of interest.

References

1. Zheng, H.; Tang, X.T.; Chen, G.; Li, Z.M. Insar baseline estimation analysis based on formation satellites. *Bulletin of Surveying & Mapping* **2009**, 35, 12-15.
2. Zhao, H.L.; Fan, J.H.; Guo, X.F. A method for insar baseline refinement and its application. Second IITA International Conference on Geoscience and Remote Sensing, Qingdao, China, 28-31 August 2010; pp 161-164.
3. Zheng, H.; Qin, X.P. Insar baseline detection based on formation satellites. *Hydrographic Surveying & Charting* **2010**, 30, 32-34.
4. Chen, G.; Tang, X.; Xuchu, Y.U.; Zheng, H. Accuracy analysis of baseline estimation algorithm of space-borne insar based on gcp. B*ulletin of Surveying & Mapping* **2009**, 27, 16-18.
5. Du, Y.; Yang, S.; Shi, H. Study on accurate estimation of baseline parameters of space-borne insar based on gcps. International Conference on Geoinformatics, Beijing, China, 18-20 June 2010; pp 1-4.

6. Jin, G.; Wu, Y.; Xiang, M.; Xu, Q.; Qin, Z. Baseline estimation algorithm of insar with block adjustment. *Acta Geodaetica Et Cartographica Sinica* **2011**, 40, 616-622.
7. Werner, C.L.; Small, D.L.; Rosen, P.A.; Hensley, S.; Zebker, H.A. Techniques and applications of sar interferometry for ers-1. Proceedings of First ERS-1 Symposium on Space at the Service of Our Environment, Washington, United States, 01 March 1993; pp205-210.
8. Singh, K.; Stussi, N.; Keong, K.L.; Hock, L. In Baseline estimation in interferometric sar, Geoscience and Remote Sensing, 1997. IGARSS '97. Remote Sensing - A Scientific Vision for Sustainable Development. *1997 IEEE International*, **1997**; 451, 454-456.
9. Xu, H.P.; Zhu, L.F.; Liu, X.H.; Chen, Y.F. A novel baseline estimation approach of spaceborne insar based on interferometric fringe frequency. *Acta Electronica Sinica* **2011**, 39, 2212-2217.
10. Fan, H.; Deng, K.; Huang, G. Study on the methods of insar baseline estimation. International Workshop on Education Technology and Training & 2008 International Workshop on Geoscience and Remote Sensing, Shanghai, China, 21-22 December 2008; pp 453-455.
11. Jin, G.W.; Qing, X.U.; Zhu, C.Y.; Han, X.L. Initial baseline estimation of insar based on the phases of flat earth. *Journal of Zhengzhou Institute of Surveying & Mapping* **2006**, 23, 231.
12. Xiao, J.; Wang, C.; Li, Z.; Yang, Y. Insar baseline estimation based on co-registration offsets. *Geomatics & Information Science of Wuhan University* **2010**, 35, 1236-1239.
13. Chen, B.; Xu, S.J.; Zhang, P. Estimation of insar baseline based on the frequency shift theory. International Conference on Radar, Shanghai, China, 16-19 October 2006; pp 1-3.
14. Ying, L.; Liao, G.S.; Lun, M.A. A baseline estimation method for insar based subspace projection. *Journal of Xidian University* **2006**, 33, 678-681.
15. Costantini, M.; Minati, F.; Quagliarini, A.; Schiavon, G. SAR interferometric baseline calibration without need of phase unwrapping. Geoscience and Remote Sensing Symposium, Anchorage, USA, 20-24 September 2004; pp 493-495.
16. Costantini, M.; Minati, F.; Quagliarini, A.; Schiavon, G. A new method for baseline calibration in sar interferometry. FRINGE Workshop, Frascati, Italy, 01-05 December 2003; pp 550-554.
17. Ferraiuolo, G.; Meglio, F.; Pascazio, V.; Schirinzi, G. Dem reconstruction accuracy in multichannel sar interferometry. *IEEE Transactions on Geoscience & Remote Sensing* **2008**, 47, 191-201.
18. Baselice, F.; Ferraioli, G.; Pascazio, V. Dem reconstruction in layover areas from sar and auxiliary input data. *IEEE Geoscience & Remote Sensing Letters* **2009,** 6, 253-257.
19. Nicolas, J.M. Insar image co-registration using the fourier–mellin transform. *International Journal of Remote Sensing* **2005**, 26, 2865-2876.
20. Jin, G.; Zhang, H.; Xu, Q. Fast one-dimensional least squares matching of insar images. IEEE International Conference on Signal Processing, Beijing, China, 24-28 October 2010; pp 1060-1063.
21. Li, D.; Zhang, Y. Geometric feature-based image co-registration approach for insar. 2009 2nd Asian-Pacific Conference on Synthetic Aperture Radar, Xian, China, 26-30 October 2009; pp 1026 - 1030.
22. Trouvé, E.; Caramma, M.; Maître, H. Fringe detection in noisy complex interferograms. *Applied Optics* **1996**, 35, 3799.
23. Lei, Y.; Qian, F.; Gang, W.Z. Optimized minimum spanning tree phase unwrapping algorithm for phase image of interferometric sar. International Conference on ITS Telecommunications Proceedings, Chengdu, China, 21-23 June 2006; pp 1240-1243.
24. Shanker, A.P.; Zebker, H. Edgelist phase unwrapping algorithm for time series insar analysis. *Journal of the Optical Society of America A Optics Image Science & Vision* **2010**, 27, 605-612.
25. Zhang, S.; Zhong, H.; Tang, J. Dendriform branch cut algorithm based on minimum spanning tree for phase unwrapping. *Procedia Engineering* **2012**, 29, 1154-1159.
26. Antony, J.W.; Gonzalez, J.H.; Schwerdt, M.; Bachmann, M.; Krieger, G.; Zink, M. Results of the tandem-x baseline calibration. *IEEE Journal of Selected Topics in Applied Earth Observations & Remote Sensing* **2013**, 6, 1495-1501.
27. Liu, Y.; Li, Z.; Yang, J.; Bao, Z. Quasi-closed-form solution for distributed satellites insar geolocation. *Journal of Xidian University* **2012**, 39, 87-93.
28. Gens, R. Sar interferometry-issues, techniques, and applications. *International J Remote Sensing* **1996**, 17, 1803-1835.
29. Hanssen, R.F. Radar interferometry data interpretation and error analysis. *Journal of the Graduate School of the Chinese Academy of Sciences* **2001**, 2, V5-577-V575-580.

30. González, J.H.; Antony, J.M.W.; Bachmann, M.; Krieger, G.; Zink, M.; Schrank, D.; Schwerdt, M. Bistatic system and baseline calibration in tandem-x to ensure the global digital elevation model quality. *Isprs Journal of Photogrammetry & Remote Sensing* **2012**, 73, 3-11.
31. Liu, Q.; Xing, S.; Wang, X.; Dong, J.; Dai, D.; Li, Y. The "slope" effect of coherent transponder in insar dem. *Progress in Electromagnetics Research* **2012**, 127, 351-370.
32. Kang, S.; Lee, D. Compensating network delays for smart actuator using lagrange polynomial curve fitting. Proceedings of SICE Annual Conference, Taibei, Taiwan, 18-21 August 2010; pp 674-677.
33. Sherman; A.H. Newton-iterative methods for the solution of systems of nonlinear equations. *Siam Journal on Numerical Analysis* **1975**, 15, 755-771.
34. Proinov, P.D. New general convergence theory for iterative processes and its applications to newton–kantorovich type theorems. *Journal of Complexity* **2010**, 26, 3-42.
35. Zhang, W.J.; Long, T. New analytic location algorithm based on spaceborne synthetic aperture radar image. *Journal of Beijing Institute of Technology* **2005**, 25, 147-150.
36. Xiang, Z.; Liu, X. Reconstruction of insar dem facilitated by orbit data and srtm data. International Conference on Signal Processing, Beijing, China, 26-29 October 2008; pp 2392-2395.
37. Guo, C.; ZHU. Studies on the dem geocoding from insar. *Modern Radar* **2003,** 1, 19-21.
38. Schwabisch, M. In A fast and efficient technique for sar interferogram geocoding, Geoscience and Remote Sensing Symposium Proceedings, 1998. IGARSS '98. *1998 IEEE International,* **1998**, 1102, 1100-1102.